Low-loss silicon nitride waveguide hybridly integrated with colloidal quantum dots

Weiqiang Xie,[1,2,*] Yunpeng Zhu,[1,2] Tangi Aubert,[2,3] Steven Verstuyft,[1,2] Zeger Hens,[2,3] and Dries Van Thourhout[1,2]

[1]*Photonics Research Group, Department of Information Technology, Ghent University-IMEC, Gent B-9000, Belgium*
[2]*Center for Nano and Biophotonics, Ghent University, B-9000 Ghent, Belgium*
[3]*Physics and Chemistry of Nanostructures, Ghent University, B-9000 Ghent, Belgium*
**weiqiang.xie@intec.ugent.be*

Abstract: Silicon nitride waveguides with a monolayer of colloidal quantum dots embedded inside were fabricated using a low-temperature deposition process and an optimized dry etching step for the composite layers. We experimentally demonstrated the luminescence of the embedded quantum dots is preserved and the loss of these hybrid waveguide wires is as low as 2.69dB/cm at 900nm wavelength. This hybrid integration of low loss silicon nitride photonics with active emitters offers opportunities for optical sources operating over a very broad wavelength range.

©2015 Optical Society of America

OCIS codes: (130.0130) Integrated optics; (230.7370) Waveguides; (160.4236) Nanomaterials.

References and links

1. E. S. Hosseini, S. Yegnanarayanan, A. H. Atabaki, M. Soltani, and A. Adibi, “High quality planar silicon nitride microdisk resonators for integrated photonics in the visible wavelength range,” Opt. Express **17**(17), 14543–14551 (2009).
2. Q. Li, A. A. Eftekhar, M. Sodagar, Z. Xia, A. H. Atabaki, and A. Adibi, “Vertical integration of high-Q silicon nitride microresonators into silicon-on-insulator platform,” Opt. Express **21**(15), 18236–18248 (2013).
3. S. Romero-García, F. Merget, F. Zhong, H. Finkelstein, and J. Witzens, “Silicon nitride CMOS-compatible platform for integrated photonics applications at visible wavelengths,” Opt. Express **21**(12), 14036–14046 (2013).
4. A. Z. Subramanian, P. Neutens, A. Dhakal, R. Jansen, T. Claes, X. Rottenberg, F. Peyskens, S. Selvaraja, P. Helin, B. Du Bois, K. Leyssens, S. Severi, P. Deshpande, R. Baets, and P. Van Dorpe, “Low-loss singlemode PECVD silicon nitride photonic wire waveguides for 532-900 nm wavelength window fabricated within a CMOS pilot line,” IEEE Photonics J. **5**(6), 2202809 (2013).
5. D. J. Moss, R. Morandotti, A. L. Gaeta, and M. Lipson, “New CMOS-compatible platforms based on silicon nitride and Hydex for nonlinear optics,” Nat. Photonics **7**(8), 597–607 (2013).
6. M. Eichenfield, R. Camacho, J. Chan, K. J. Vahala, and O. Painter, “A picogram- and nanometre-scale photonic-crystal optomechanical cavity,” Nature **459**(7246), 550–555 (2009).
7. M. Khan, T. Babinec, M. W. McCutcheon, P. Deotare, and M. Loncar, “Fabrication and characterization of high-quality-factor silicon nitride nanobeam cavities,” Opt. Lett. **36**(3), 421–423 (2011).
8. K. Luke, A. Dutt, C. B. Poitras, and M. Lipson, “Overcoming Si_3N_4 film stress limitations for high quality factor ring resonators,” Opt. Express **21**(19), 22829–22833 (2013).
9. X. Tu, J. Song, T. Y. Liow, M. K. Park, J. Q. Yiying, J. S. Kee, M. Yu, and G. Q. Lo, “Thermal independent silicon-nitride slot waveguide biosensor with high sensitivity,” Opt. Express **20**(3), 2640–2648 (2012).
10. L. Martiradonna, T. Stomeo, M. De Giorgi, R. Cingolani, and M. De Vittorio, “Nanopatterning of colloidal nanocrystals emitters dispersed in a PMMA matrix by e-beam lithography,” Microelectron. Eng. **83**(4–9), 1478–1481 (2006).
11. Y. K. Olsson, G. Chen, R. Rapaport, D. T. Fuchs, V. C. Sundar, J. S. Steckel, M. G. Bawendi, A. Aharoni, and U. Banin, “Fabrication and optical properties of polymeric waveguides containing nanocrystalline quantum dots,” Appl. Phys. Lett. **85**(19), 4469 (2004).
12. I. Suárez, H. Gordillo, R. Abargues, S. Albert, and J. Martínez-Pastor, “Photoluminescence waveguiding in CdSe and CdTe QDs-PMMA nanocomposite films,” Nanotechnology **22**(43), 435202 (2011).
13. C. A. Foell, E. Schelew, H. Qiao, K. A. Abel, S. Hughes, F. C. J. M. van Veggel, and J. F. Young, “Saturation behaviour of colloidal PbSe quantum dot exciton emission coupled into silicon photonic circuits,” Opt. Express **20**(10), 10453–10469 (2012).
14. M. Humer, R. Guider, W. Jantsch, and T. Fromherz, “Integration, photostability and spontaneous emission rate enhancement of colloidal PbS nanocrystals for Si-based photonics at telecom wavelengths,” Opt. Express **21**(16), 18680–18688 (2013).
15. S. Gupta and E. Waks, “Spontaneous emission enhancement and saturable absorption of colloidal quantum dots coupled to photonic crystal cavity,” Opt. Express **21**(24), 29612–29619 (2013).

16. A. Qualtieri, F. Pisanello, M. Grande, T. Stomeo, L. Martiradonna, G. Epifani, A. Fiore, A. Passaseo, and M. De Vittorio, “Emission control of colloidal nanocrystals embedded in Si_3N_4 photonic crystal H1 nanocavities,” Microelectron. Eng. **87**(5–8), 1435–1438 (2010).
17. A. Gorin, A. Jaouad, E. Grondin, V. Aimez, and P. Charette, “Fabrication of silicon nitride waveguides for visible-light using PECVD: a study of the effect of plasma frequency on optical properties,” Opt. Express **16**(18), 13509–13516 (2008).
18. Y. Justo, I. Moreels, K. Lambert, and Z. Hens, “Langmuir-Blodgett monolayers of colloidal lead chalcogenide quantum dots: morphology and photoluminescence,” Nanotechnology **21**(29), 295606 (2010).
19. B. De Geyter, K. Komorowska, E. Brainis, P. Emplit, P. Geiregat, A. Hassinen, Z. Hens, and D. Van Thourhout, “From fabrication to mode mapping in silicon nitride microdisks with embedded colloidal quantum dots,” Appl. Phys. Lett. **101**(16), 161101 (2012).
20. R. A. Morgan, *Plasma Etching in Semiconductor Fabrication* (Elsevier Press, 1985), Chap. 3.
21. J. W. Coburn, “Insitu Auger electron spectroscopy of Si and SiO_2 surfaces plasma etched in CF_4-H_2 glow discharges,” J. Appl. Phys. **50**(8), 5210–5213 (1979).
22. J. W. Coburn and H. F. Winters, “Plasma etching—a discussion of mechanisms,” J. Vac. Sci. Technol. **16**(2), 391–403 (1979).
23. V. Srivastav, R. Pal, and H. P. Vyas, “Overview of etching technologies used for HgCdTe,” Opto-Electron. Rev. **13**(3), 197–211 (2005).

1. Introduction

Silicon nitride (SiN) exhibits transparency from the visible to the mid-infrared and has a fairly high optical index (~2.0), making it suitable for various photonic applications including integrated photonic circuits [1–4], nonlinear optics [5], high quality optical cavities [6–8], and on-chip biosensing [9]. On the other hand, because of its dielectric nature, the SiN platform is thus far limited to passive devices and a light source such as a laser or a single photon emitter integrated in this platform is highly desired. Colloidal quantum dots (QDs), with their efficient luminescence, tunable from the visible to the infrared wavelength, potentially could be used as the emitters in photonic applications. In fact, colloidal QDs have already been integrated with various types of photonic integrated circuits (PIC), including polymer matrix and waveguides [10–12], silicon photonic circuits [13, 14] and SiN nanocavities [15]. In all these examples, the QDs were either stabilized in a polymer matrix or directly dispersed on the surface of the devices. Given the drawbacks of the polymers used (low index contrast, unknown long term stability) and the instability of the QDs themselves when they are left exposed, there is a need for the integration of colloidal QDs with an all inorganic low-loss PIC-platform whereby the QDs are fully encapsulated. Furthermore, given the wide tunability of colloidal QDs – e.g. by changing their diameter and/or the materials used – it is important also the waveguide platform used is capable of handling a wide range of wavelengths. SiN provides this wide tunability and therefore its integration with QDs forms a promising route to achieve this goal. For practical applications, it is important that the QDs are well stabilized within the SiN layers used for realizing the waveguides, using a process that does not affect the optical properties of the QDs and while still allowing realizing high performance optical circuits. In addition it is important that the geometrical pattern of the embedded QD film and its location can be controlled precisely with respect to the targeted optical devices. Although, colloidal QDs have been embedded in SiN photonics [16], there is still a lack of quantitative evaluation of this hybrid photonic platform in terms of optical losses and optimal fabrication process.

In this work, we developed a low-loss hybrid SiN-QD photonic platform based on a low-temperature (120-270°C) plasma enhanced chemical vapor deposition (PECVD) process. By using an optimized dry etching process, we fabricated waveguides with a close-packed monolayer of colloidal QDs embedded into two layers of SiN, of which the top layer was deposited at 120°C to maximally preserve the luminescence of the QDs. At 900nm wavelength a loss as low as 2.69dB/cm is demonstrated for these hybrid waveguides. Since only standard lithography and direct top-down etching is utilized here, one could envisage leveraging mature complementary metal-oxide-semiconductor (CMOS) technology for the realization of active SiN devices, e.g. high quality factor cavities with embedded QDs. Therefore the present hybrid SiN-QD platform provides a promising solution for the integration of optical emitters with the fully inorganic SiN photonic platform.

2. Mask design and fabrication

The test pattern designed contains waveguides with widths varying from 0.8μm to 2.0μm, each width having a straight reference waveguide and spiral waveguides with a series of lengths 1, 2, 4, and 8cm for cut-back measurements. The bend radius of the spiral waveguides is fixed at 100μm, for which the bending loss is negligible according to numerical simulations [3]. Away from the spiral part, both sides of the waveguides are tapered to 3.0μm to facilitate easier facet cleaving and reproducible coupling to and from the chip. The fabrication includes substrate preparation and waveguide definition, as shown in the process flow in Fig. 1(a).

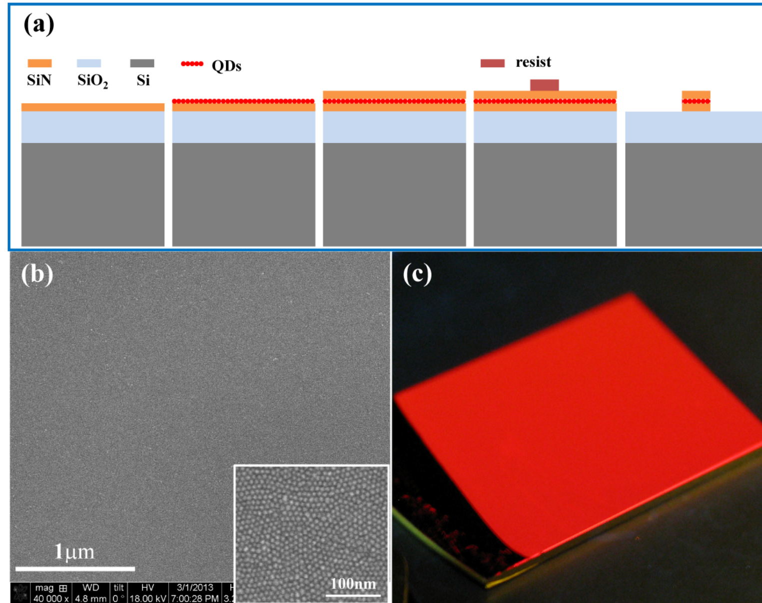

Fig. 1. (a) Schematics of SiN/QDs/SiN hybrid waveguide fabrication flow. (b) SEM image of the LB QD-film with the inset showing the close-packed LB QD-film under a high resolution. (c) PL of a 2cm × 2cm LB QD-film illuminated with a UV lamp.

Firstly we prepared a SiN/QDs/SiN sandwich substrate starting with a silicon wafer with a 3μm thermal SiO_2 box layer, onto which first a 100nm SiN layer was deposited using an optimized PECVD process at a temperature of 270°C. A low plasma frequency was chosen to have a low optical loss of the material [17]. Next a close-packed monolayer of colloidal QDs was transferred onto the SiN substrate by a Langmuir–Blodgett (LB) method [18]. We used CdSe/CdS core/shell QDs, a typical visible-emission colloidal QD-type, with a diameter of ~7.2nm and a central emission peak of ~625nm. The quality of the QD-film was examined by scanning electron microscope (SEM) and photoluminescence (PL) under a UV lamp, as presented in Figs. 1(b) and 1(c), showing the layer of QDs is uniform over large areas. A second 100nm SiN layer was subsequently deposited for embedding the LB QDs layer, using the same PECVD process. In this case a lower temperature (120°C) was used however to minimize impact on the optical quality of the QDs [19], while still retaining sufficient material quality for the SiN to allow for low-loss photonic devices. This is confirmed by ellipsometry measurements where, within the measurement accuracy, we do not see a difference in the extinction coefficient of SiN deposited at 120°C compared to that deposited at 270°C. The refractive index on the other hand (measured at 900nm) changes from 1.92 to 1.85 with the temperature decreasing from 270°C to 120°C, indicating a reduction in the material density. After preparation of the substrate, the photoresist mask for the waveguides was patterned using contact optical lithography, and the resist process was optimized to have a steep and smooth sidewall, which is critical for the subsequent dry etching process. Finally,

the waveguide pattern was transferred into the SiN layers by using reactive ion etching (RIE) to form strip waveguides. For simplicity, hereafter the terms H-SiN and L-SiN will be used to refer to SiN deposited at 270°C and at 120°C respectively. In order to evaluate the influence of the deposition temperature on the optical quality of the SiN devices, we also fabricated waveguides using a single deposition of 200nm H-SiN and L-SiN, respectively. Similarly, next to the H-SiN/QDs/L-SiN stacks, also an H-SiN/L-SiN stack without QDs was prepared to compare the etch behavior and waveguide loss of structures with and without embedded QDs.

3. Optimization of dry etching for H-SiN/L-SiN and H-SiN/QDs/L-SiN waveguides

Achieving low loss waveguides in the layer stacks introduced above requires vertical and smooth sidewalls and therefore we need optimization of the RIE conditions. Various plasma chemistries, such as CF_4 [1], CF_4/CHF_3 [2], $C_4F_8/SF_6/H_2$ [7], CHF_3/O_2 [8], and CF_4/H_2 [16], have already been used to obtain anisotropic etching in SiN. However, unlike what is the case for SiN-films deposited in a single step, due to the considerable difference in material density the etching behavior between H-SiN and L-SiN deposited on top of each other can vary a lot. As a result, the standard etching processes described in literatures result in a stepwise transition at the interface, which can lead to uncontrolled waveguide dimensions and additional losses. An optimized process should be sufficiently anisotropic and can passivate the sidewalls such that those are not etched during the process, resulting in topologically united sidewall surfaces. Moreover, the roughness of the etched sidewalls should be minimized to reduce the associated scattering loss in waveguide. Further, for etching of the H-SiN/QDs/L-SiN stack, the process should be capable of etching through a QD film, guaranteeing the etching does not stop on this layer and vertical sidewalls are obtained. In this study, we adopted CF_4 as the basic etchant gas and added O_2 and H_2 to adjust the etch profile. The experiments were carried out in an Advanced Vacuum Vison 320 RIE tool. To maintain a moderate etch rate the plasma power was fixed at 210W, and the chamber pressure was optimized and kept at 20mTorr. The gas rates and ratios were systematically studied with the goal of obtaining vertically etched sidewalls and smooth surfaces. The etched samples were inspected by SEM analysis on focused ion beam (FIB) milled cross-sections. In order to avoid excessive charging effects, we carried out the initial etching experiments and the corresponding SEM check on SiN-films deposited on bare silicon substrates without the insulating SiO_2 buried oxide layer. This resulted in considerably better pictures and allowed inspecting both the etched profile and surface roughness with higher resolution.

First, to investigate the influence of the gas composition on the degree of anisotropy, we etched an H-SiN/L-SiN stack with pure CF_4 and then added either O_2 or H_2 for comparison. In Figs. 2(a)-2(c) we show FIB-defined cross-sectional images of the H-SiN/L-SiN films etched with CF_4 (40sccm), CF_4/O_2 (40sccm/3sccm), and CF_4/H_2 (40sccm/3sccm), respectively.

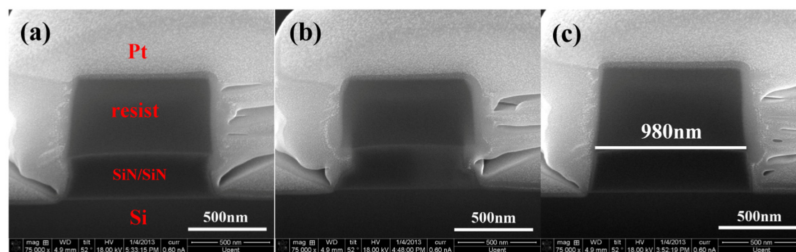

Fig. 2. FIB cross-sectional images of the as-etched H-SiN/L-SiN waveguide with a designed width of 1.0μm and a total thickness of 300nm. The etching gases are (a) CF_4 (40sccm), (b) CF_4/O_2 (40sccm/3sccm), and (c) CF_4/H_2 (40sccm/3sccm).

Note that the resist mask was retained during SEM examination for verifying the reliability of the contact lithography process. Pure CF_4, as shown in Fig. 2(a), etches both SiN

layers primarily in the vertical direction but there is also considerable lateral etching resulting in a curved profile. To adjust the etched profile, we first added a small amount of O_2 to the CF_4 flow. The result is shown in Fig. 2(b), showing that the presence of O_2 results in a more isotropic etching of the L-SiN layer with strong undercutting of the resist mask. At the interface between both SiN layers a strong step is visible indicating that the L-SiN and H-SiN exhibit significantly different etch rates in horizontal direction. This enhanced isotropic etching results from the increasing concentration of fluorine radicals together with the lack of sidewall protection which is removed in the presence of the O_2 plasma [20]. The impact is stronger for the L-SiN layer. As a consequence the horizontal etch rate difference between L-SiN and H-SiN is increased, leading to a step at the interface. The variation in horizontal etching rate between the L-SiN and H-SiN layers is a further manifestation of the distinct change in their material density and of the need for a nearly complete anisotropic etching process for obtaining vertical sidewalls with a continuous surface. In Fig. 2(c), we present the etched profile when using a gas mixture of CF_4/H_2 which shows the desired straight sidewall with a united surface, albeit with a slight slope. This significant improvement can be attributed to a greatly increased anisotropic etching occurring due to the formation of a protective polymer layer on the sidewalls in the presence of H_2 [21, 22]. This polymer layer inhibits etching of the lateral surfaces whereas on the bottom surface it is removed by the directional ion bombardment leaving it fully exposed to reactive species. Accordingly the process is dominated by the vertical etching component and there is hardly any lateral etching. In Fig. 2(c), it is also obvious that the resist mask has a steep sidewall and that the dimension of the designed feature is faithfully transferred into the SiN stack, demonstrating the suitability of our contact optical lithography for defining a dry etching mask.

In order to further improve the etch profile in terms of sidewall slope and surface roughness, we adjusted the CF_4/H_2 ratio in the process using values of 40sccm/3sccm, 60sccm/3sccm, and 80sccm/3sccm for the respective gas flows (Fig. 3). When increasing the proportion of CF_4 in the system, the slope of the etched sidewall is gradually tuned from a positive profile to a vertical one as obvious in Figs. 3(a)-3(c). More importantly, the roughness of the sidewall is reduced by increasing the ratio of CF_4 to H_2. The effect of the

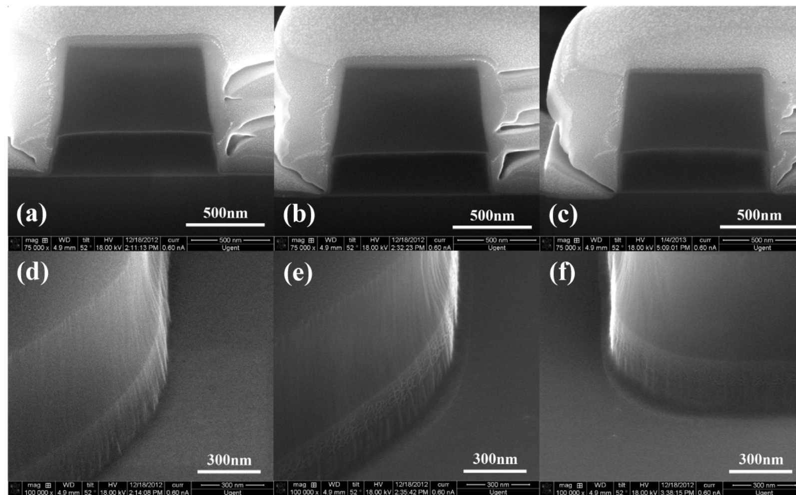

Fig. 3. FIB cross-sectional and sidewall images of the as-etched H-SiN/L-SiN layers. The gas system is CF_4/H_2 with different ratios of (a, d) 40sccm/3sccm, (b, e) 60sccm/3sccm, and (c, f) 80sccm/3sccm.

CF_4/H_2 ratio on the sidewall slope originates from the competition between the etching process and the polymer inhibitor deposition [22]. At proportionally higher hydrogen flows (CF_4/H_2 ratio of 40sccm/3sccm) there is an excess deposition of the polymer inhibitor on the

lateral surface where it is not removed by the vertical ion bombardment, resulting in a sloped profile and a much rougher surface as shown in Figs. 3(a) and 3(d). As an extreme example of this effect, when increasing the H_2 flow rate to 20sccm no etching at all occurs. By reducing the hydrogen content (CF_4/H_2 ratio of 80sccm/3sccm) the fine balance between etching and deposition results in a vertical sidewall and an improved surface roughness, as shown in Fig. 3(c). When further increasing the CF_4 flow the profile tends toward the profile obtained using pure CF_4, shown in Fig. 2(a).

Next, we optimized the etching process for the layers stack containing the QDs, using the optimized etch condition for the H-SiN/L-SiN layer stack (CF_4/H_2 of 80sccm/3sccm) as the starting point. The result is shown in Figs. 4(a) and 4(b). Apparently, this RIE process does indeed allow etching through the close-packed monolayer of CdSe/CdS QDs, most probably through the formation of volatile organometallic etch products in the CF_4/H_2 plasma [23]. However, due to the slight quality loss of the L-SiN when deposited on the QD layer, this etching process results in an unwanted undercut at the interface of L-SiN and QDs, leaving an observable step. As discussed above, increasing the hydrogen content in the gas mixture should help protecting the L-SiN against lateral etching. In Figs. 4(c) and 4(d), we show the as-etched results using a CF_4/H_2 ratio of 40sccm/3sccm. The profile is clearly improved as expected. The sidewall is etched almost vertically and exhibits a topologically continuous surface without distinct roughness. In Figs. 4(c) and 4(d) also the embedded QD layer is visible. No defects along the uniform monolayer are visible indicating the high quality of the LB process used for preparing the layer and the fact that the dry etching process does not attack the layer. Summarizing, we have obtained optimized etching conditions for pure SiN and hybrid SiN/QDs waveguides with CF_4/H_2 ratios of 80sccm/3sccm and 40sccm/3sccm, respectively, under a fixed plasma power of 210W and a chamber pressure of 20mTorr.

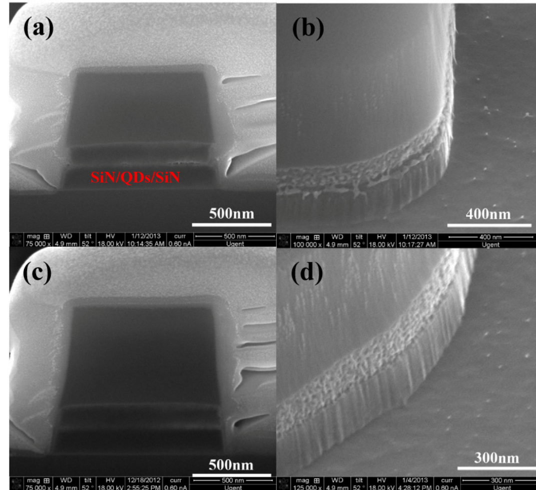

Fig. 4. FIB cross-sectional and sidewall images of the as-etched H-SiN/QDs/L-SiN layers. The gases ratio of CF_4/H_2 in (a, b) and (c, d) are 80sccm/3sccm and 40sccm/3sccm, respectively.

4. Measurement and discussion

4.1 Fabricated SiN and hybrid SiN/QDs waveguides and PL characterization

Both pure SiN and hybrid SiN/QDs waveguides were fabricated using the optimized etching processes discussed above. In Figs. 5(a) and 5(b), we show cross-sectional photographs of 2μm-wide waveguides defined in H-SiN/L-SiN and H-SiN/QDs/L-SiN structures deposited on a 3μm oxide layer. Both types of waveguides consist of a ~100nm bottom H-SiN layer and a ~100nm top L-SiN layer. In the case of the hybrid H-SiN/QDs/L-SiN waveguide, a monolayer of QDs is embedded between the two layers of SiN (not clearly visible in Fig. 5(b)

due to charging in the SEM). The H-SiN/L-SiN waveguide in Fig. 5(a) exhibits a vertical sidewall while the sidewall of the H-SiN/QDs/L-SiN waveguide shows a slightly sloped profile, in line with the observations discussed in the previous section and demonstrating the reproducibility of our process. As the QDs in the H-SiN/QDs/L-SiN stack were subject to a PECVD deposition at 120°C, their optical quality could have been degraded. In order to verify this, we measured the PL of QDs after embedding them in an H-SiN/QDs/L-SiN waveguide and compared it with that of patterned QDs processed at room temperature on top of a SiN waveguide. The result is shown in Fig. 5(c). In both cases, the PL was excited by illuminating the top of the waveguide with a 447nm laser diode and then collected from the cleaved facet of a waveguide with a microlensed fiber. It can be seen that, except for a red shift and an increased emission at longer wavelength probably due to an increased trap emission, the main features of the PL spectrum are well preserved. Because of different pumping and collecting efficiencies, it is hard to compare the absolute PL intensities of embedded QDs with those deposited on top of the SiN film. Therefore in Fig. 5(c) we only show the normalized PL. As demonstrated in our previous work [19], in general there is a reduction in PL intensity after depositing SiN at 120°C, and this effect is dramatically magnified when increasing temperature (e.g. to 300°C). We believe that by further improving the quality of the QDs themselves, e.g. by increasing the shell thickness for better protection of the core, the wavelength shift and intensity decrease of the PL can further be decreased.

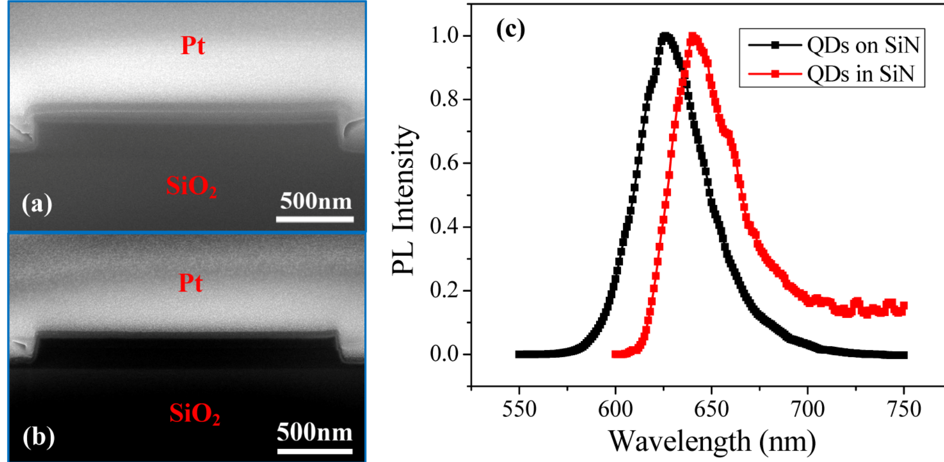

Fig. 5. FIB cross-sectional images of ~200nm-thick, 2μm-wide waveguides for (a) H-SiN/L-SiN and (b) H-SiN/QDs/L-SiN structures on 3μm oxide box. (c) Normalized PL intensity of QDs on the top of SiN and embedded in SiN waveguides, respectively.

4.2 Loss measurement for SiN and hybrid SiN/QDs waveguides

To evaluate the processes introduced above more quantitatively, we measured the propagation losses of SiN and SiN/QDs waveguides. We used a cut-back method with spiral waveguides of different lengths, and the losses were extracted by fitting the length-dependent fiber-to-fiber transmission. This method assumes constant coupling conditions for waveguides with identical design but varying lengths. We measured the coupling uncertainty to be below 1.5 dB, which, considering the longest spiral waveguide is 8 cm, results in an upper limit for the error in the measured losses of less than 0.2dB/cm. The measurement was carried out using a near-infrared tunable laser using end-fire coupling from microlensed fibers coupled in and out to the cleaved facets of the waveguide. The transmitted power is maximized with a polarizer resulting in excitation of the TE-like modes, which have lower loss than the TM-like modes. As mentioned before, the target of this work is to develop and demonstrate a SiN-QD compatible technical platform integrating low-loss passive photonics with efficient photon emitters inside. Of primary concern is the optimization of the fabrication process, especially

the deposition and etching, and their influence on the waveguide quality. Therefore we measured the waveguide losses at a wavelength of 900 nm to avoid the intrinsic absorption peak of the QD layer and hence the measured loss mainly originates from absorption loss in the SiN layers, scattering loss by surface roughness and non-uniformity in the QD layer and other loss caused by fabrication imperfections.

To investigate the influence of the deposition temperature, we fabricated H-SiN and L-SiN waveguides and compared their loss. The results are plotted as function of the designed waveguide width in Fig. 6(a). For both cases, the losses rapidly decline for widths increasing from 0.8μm to 1.2μm and then exhibit a more gradual decrease for widths varying from 1.0μm to 1.5μm. The relatively larger losses and fitting errors at widths of 0.8μm and 0.9μm for both H-SiN and L-SiN waveguides can be attributed to the fact that the deviation of dimension and the imperfection of fabrication in our optical lithography become more significant when the feature size decreases below 1.0μm, resulting in considerable losses. When further increasing the width to 2.0μm, the losses for H-SiN and L-SiN saturate to 0.94 dB/cm and 1.88dB/cm, respectively. The inset of Fig. 6(a) shows the transmission of the 2.0μm-wide waveguides for different lengths and the corresponding linear fits. The small discrepancy between the measured and fitted results clearly demonstrates the reliability of the cut-back method for determining the waveguide loss. It is interesting to note that for all widths L-SiN waveguides have about two times the loss of the H-SiN waveguides, which can be understood from the differences in material quality and sidewall etching. While for smaller widths the effect of sidewall roughness dominates the waveguide loss, for wider waveguides and in particular for the 2.0μm wide waveguides, which support also higher order TE-modes at wavelengths of 900 nm, the material absorption and the scattering within the waveguide become more important. This leads us to conclude that the L-SiN layer exhibits an intrinsically higher material loss than the H-SiN layer deposited at higher temperature. Nevertheless, we choose L-SiN as the top layer for embedding QDs in a hybrid SiN/QDs/SiN waveguide, given the fact that the optical quality of the QDs is maximally preserved when limiting the process temperature [19].

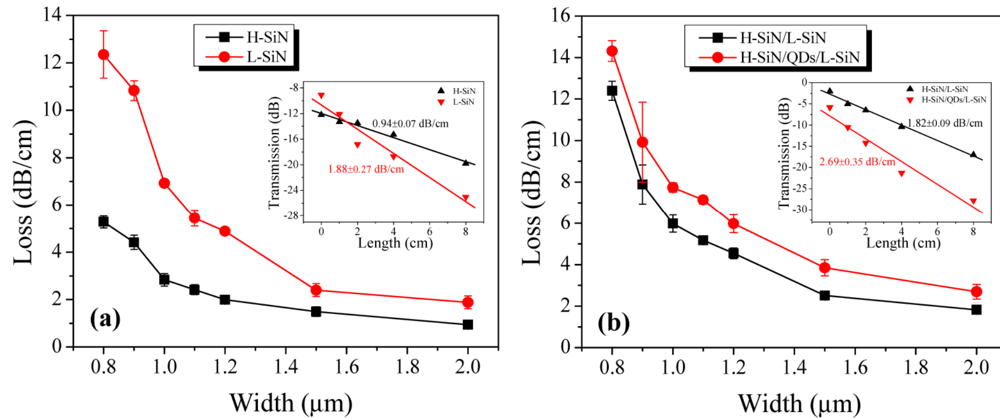

Fig. 6. Waveguide losses at different widths of single deposit H-SiN and L-SiN layer in (a) and H-SiN/L-SiN and H-SiN/QDs/L-SiN stacked layers in (b), obtained by linearly fitting waveguide-length dependent transmission. The insets in (a) and (b) show the transmissions of 2μm-wide waveguide at different lengths together with the corresponding linear fits of the slopes for different types of waveguide, indicating a very small discrepancy between the measured and fitted results.

To investigate the effect of embedding the QD layer in the waveguide we prepared both H-SiN/L-SiN and H-SiN/QDs/L-SiN waveguides and measured their loss as function of the waveguide width. The results shown in Fig. 6(b) show a similar decrease in loss for wider waveguides as discussed above for the H-SiN and L-SiN waveguides. We obtain losses as low as 1.82dB/cm and 2.69dB/cm for the widest H-SiN/L-SiN and H-SiN/QDs/L-SiN

waveguides, respectively. The inset again shows the transmission as function of length for these 2.0μm wide waveguides and the associated linear fits. However, unlike the significant difference of loss seen in Fig. 6(a) between H-SiN and L-SiN waveguides, the loss of the H-SiN/QDs/L-SiN waveguide stably remains 1-2dB/cm larger than that of the H-SiN/L-SiN waveguide for all measured widths as seen in Fig. 6(b). It is clear that this loss difference comes from the presence of QDs in the H-SiN/QDs/L-SiN waveguides. As shown in the previous section, the sidewalls of the H-SiN/QDs/L-SiN waveguide are slightly sloped and a bit rougher than those of the waveguides without embedded QDs. In addition, the QD layer can introduce some roughness at the interfaces of the layer deposited on top, e.g. due to the imperfections in the LB deposited QD layer. All of these could account for the 1-2 dB/cm increase in loss for the H-SiN/QDs/L-SiN waveguides compared to the H-SiN/L-SiN waveguides. It is expected that using a more advanced lithography process, e.g. using DUV-lithography instead of contact mask lithography, should reduce dimensional fluctuations along the waveguide and fabrication imperfections, leading to even lower losses, in particular for the single-mode waveguides with widths less than 1.2μm.

5. Conclusion

In this paper, we developed a platform for the hybrid integration of SiN photonics with colloidal QDs. Through optimization of the dry etch process, we demonstrated a loss as low as 0.94dB/cm for SiN waveguide deposited at 270°C and a loss of 1.88dB/cm for layers deposited at 120°C. Furthermore, hybrid waveguides consisting of a close-packed monolayer of QDs embedded in between SiN layers were fabricated, enabled by the low temperature deposition process, here used for the top SiN-layer, and by a further optimized etch process. Compared to processes whereby the QD-film and SiN-film would be separately defined, the process presented here allows for perfect alignment of the QD pattern with respect to the waveguide devices. This is of particular importance for high quality factor whispering gallery cavities where the optical mode is located directly near the etched interfaces. Measurements of the photoluminescence and the waveguide transmission proved not only that the QDs retain their optical quality but also that these hybrid waveguides can be defined with losses lower than 2.7dB/cm. Since the entire fabrication of SiN/QDs waveguide wires is CMOS compatible, the present platform can take advantages of existing CMOS technology and enable realizing on-chip low-loss SiN devices integrated with active QDs. This SiN/QDs hybrid waveguide, with its excellent emission properties and low losses forms a promising building block for the realization of compact integrated active SiN-based photonic devices relying fully on inorganic materials.

Acknowledgment

The authors acknowledge the ERC-ULPPIC and the IAP Photon@BE projects for financial support.